Thin film mediated and direct observation of LIPSS on soda-lime glass by femtosecond IR laser beam

K. Deva Arun Kumar, Alex Capelle, Wael Karim, Herve Rabat, Loic Gimenez, Barthélemy Aspe, Amaël Caillard, Martin Depardieu, Anne-Lise Thomann, Nadjib Semmar

Optics and Lasers in Engineering 180 (2024) 108321

Contents lists available at ScienceDirect

Optics and Lasers in Engineering

journal homepage: www.elsevier.com/locate/optlaseng

Thin film mediated and direct observation of LIPSS on soda-lime glass by femtosecond IR laser beam

K. Deva Arun Kumar [a], Alex Capelle [a], Wael Karim [a], Herve Rabat [a], Loic Gimenez [a], Barthélemy Aspe [a], Amaël Caillard [a], Martin Depardieu [b], Anne-Lise Thomann [a], Nadjib Semmar [a,*]

[a] Groupe de Recherches sur l'Énergétique des Milieux Ionisés, GREMI, Université d'Orléans, CNRS, 14 Rue d'Issoudun, 45067, France
[b] Décor World Services (DWS), 1 Av. du Champ de Mars, 45100 Orléans, France

ARTICLE INFO

Keywords:
Soda-lime glass substrate
Laser-induced periodic surface structures (LIPSS)
Femtosecond laser irradiation
Repetition rate
HSFL and LSFL

ABSTRACT

In this work, we present an new approach for creating laser-induced periodic surface structures (LIPSS) on a soda-lime glass using a femtosecond (fs) laser source, marking the first instance of such a process. The formation of LIPSS upon irradiation with linearly polarized fs-laser pulses ($\tau = 300$ fs, $\lambda = 1030$ nm) in the air environment is experimentally studied. Due to the nonlinear absorption behavior of the fs-laser beam in soda-lime glass, we conducted three different investigations to irradiate the glass substrate: (i) thin film-mediated LIPSS under top material irradiation, (ii) thin film-mediated LIPSS under bottom material irradiation, and (iii) LIPSS on glass substrate under bottom material irradiation. In the first case, High Spatial Frequency-LIPSS (HSFL) are observed, with parallel orientation to the laser beam polarization (**E**), across four different repetition rates or frequencies (f): 10 kHz, 50 kHz, 100 kHz, and 250 kHz. Additionally, the scan-axis alignment with the laser beam polarization significantly influences the uniformity of the generated LIPSS along the scan line. Redeposition is observed when the scan axis is parallel to the laser beam polarization, as compared to the perpendicular direction. In the second case, simultaneous formation of parallel (HSFL) and perpendicular Low Spatial FrequencyLIPSS (LSFL) to the laser beam polarization was highlighteded, exhibiting periods ranging from 200 nm to 550 nm for bottom irradiation. This observation occurs as the repetition rate varies between 10 kHz to 250 kHz. In the third case, we observed the LSFL formation without thin film layer on soda-lime glass material (bottom irradiation) when utilizing the maximum repetition rate $f = 250$ kHz. A notable alteration in the spatial period (545 nm - 585 nm) upon adjusting the focal distance (71 mm - 72 mm) between the substrate and the focal lens was evidenced. A possible mechanism of LIPSS formation has been discussed in the three different cases. The observation of regularly distributed LIPSS holds promise for applications in optics, microfluidics, photovoltaics, and biomaterials.

1. Introduction

The selection of glass materials is crucial for a wide range of high-tech applications, including optics, solar cells, microfluidics, and biomaterials [1]. It is worth noting that their surface-specific properties, including absorption, reflection, and wettability, can be finely tuned through surface engineering. The most prevalent type is soda-lime glass, known for its cost-effectiveness and remarkable stability, along with favorable mechanical properties [2]. The CO_2 laser can be used for rapid processing for surface modification with an efficient laser source that is capable of operating as a continuous wave at high power, also the long-wavelength infra-red (LWIR) region [3]. This highly flexible CO_2 laser can be utilized in both industrial-scale production and smaller-scale laboratories for glass modification. In thin film patterning, short pulse lasers ranging from nanoseconds to femtoseconds in duration have conventionally been preferred [4]. Because of their exceptionally short-pulse durations, femtosecond lasers utilize multiphoton absorption and electron plasma for material removal [5,6]. In general, mechanisms involved with picosecond and nanosecond lasers are thermal ablation, phase explosion, and photo-thermal effects, which arise due to their extended pulse durations [7]. Although, femtosecond lasers provide superior precision with minimal thermal damage, nanosecond

* Corresponding author.
E-mail address: nadjib.semmar@univ-orleans.fr (N. Semmar).

https://doi.org/10.1016/j.optlaseng.2024.108321
Received 23 March 2024; Received in revised form 6 May 2024; Accepted 12 May 2024
Available online 23 May 2024

lasers may induce more defects or alterations of the material properties. Moreover, femtosecond (fs) lasers have been established as a versatile tool for creating functional structures within transparent materials (nano gratings) [8], as well as on the surfaces of various materials [9].

Understanding the spontaneous appearance of patterns on laser-irradiated surfaces has been a topic of interest for many years. The possibility of obtaining micro and sub-micrometric structuring on various substrates using laser irradiation tools has drawn global attention to the generation of laser-induced periodic surface structures (LIPSS). Over the past decade, there has been a notable surge in attention towards LIPSS [10], despite their first observation by Birnbaum on a semiconducting material surface in 1965 [11]. LIPSS have a significant impact on various application fields, primarily associated with enhancing surface functionalities such as hydrophobicity, optical properties, and cellular differentiation [12,13]. Typically, LIPSS can be induced by the presence of ultra-short laser sources (like ps and fs), and these spatial periods (Λ) are significantly closer to or smaller than the laser irradiation wavelength (λ) used [14–16]. When irradiating solids with linearly polarized fs-laser pulses in air at normal incidence, typically two distinct types of LIPSS are observed, Low Spatial Frequency LIPSS (LSFL) and High Spatial Frequency LIPSS (HSFL), aligned either parallel or perpendicular to the polarization **E** of the laser beam. Numerous experimental parameters have been recognized as crucial factors for LIPSS generation, such as laser wavelength (λ), beam polarization (**E**), angle of incidence, bandgap, repetition rate (f) and two key parameters: the laser fluence (F) (energy density in J/cm^2) and the number of laser pulses (N) applied in the same area (static mode), that contribute to the energy dose evaluation by accumulation, absorbed by the material surface [17–20].

In recent decades, many works have been published based on the approach of LIPSS generation by ultra-short pulses laser systems on metal, semiconductors, and selected observations on dielectric materials. J. Bonse et al. [19] reported LIPSS generation on different materials such as metal (titanium), semiconductor (silicon), and dielectric (fused silica), which were chosen as substrates to investigate a wide range of optical bandgap values. In particular, recent studies have been conducted on the formation of LIPSS in air environment upon fs-laser pulse irradiation in dielectric substrates, especially focusing on fused silica [21–24]. Most of the studies observed HSFL on dieletric materials with spatial period sizes ranging from 75 nm to 350 nm, while the LSFL periods ranged between 500 nm and 800 nm [21,23,24]. The investigation into LIPSS formation on glass materials becomes more exciting when considering the exploration of various parameters such as wavelength, laser pulse count, fluence, and beam polarization. Although, various glasses may share similar optical properties, the formation of LIPSS is primarily influenced by the chemical composition of the glasses, especially their respective viscosities [25].

Recently, Stephan Gräf et al. [25] reported the systematic investigation of LIPSS formation on dielectric materials (or high gap glasses) such as fused silica, borosilicate glass, and soda-lime-silicate glass using fs-laser radiation by changing different parameters of fluence, number of pulses, and repetition rate. They have observed the presence of both LSFL and HSFL on fused silica and borosilicate glass substrates. However, in the case of soda-lime-silicate glass, the LIPSS are remarkably occured in the material melt phase and the HSFL are hardly visible at low fluence, $F = 3.3$ J/cm^2. At the highest fluence, $F = 14.6$ J/cm^2, the melting process is strongly promoted and the material surface of the ablated area is completely flat without the presence of any LIPSS-like surface. To the best of our knowledge, there is still no observation of LIPSS on the soda-lime glass due to its strong non-linear absorption and melt formation behaviors.

In this contribution, we examine the current research state in the field of LIPSS generation on both sides (top and bottom irradiation) by fs-laser pulses in an atmospheric environment. The key innovation in this study is the utilization of external copper tape (double side tape) placed between the glass surface and the sample holder, which plays a crucial role in generating LIPSS due to facilitating the formation of Surface Plasmon Polaritons (SPPs) via copper ions. We also explore the generation of LIPSS on soda-lime glass mediated by a thin film (Ag + Cr) layer. In this case, the metal thin film plays an essential role in creating LIPSS through the excitation of SPPs (interface between air and film) as reported by Juraj Sladek et al. [26]. The proposed mechanism for transitioning from HSFL formed at low repetition rates to LSFL, which are characteristic of high repetition rates, is also discussed.

2. Materials and methods

To investigate the LIPSS formation on wide bandgap materials, we opted to use a dielectric substrate (soda-lime glass). This choice is based on the expectation of a significant contrast between the optical properties of dielectric materials (non-linear absorption), and those of strong absorption materials such as metals or semiconductors. We selected a high-purity soda-lime glass (with an energy bandgap of E_g= 3.9 eV) made from a dielectric transparent material (Suprasil, Hanau, Germany). We recently reported the photograph and chemical composition of the chosen soda-lime glass bottle [27]. The chemical composition of the soda-lime glass was determined using X-fluorescence, and the results are presented in Table 1.

Perior to the laser processing, the material was precision-cut into a rectangular shape measuring 20 × 20 × 3 mm^3. The glass substrate experienced ultrasonic cleaning in both acetone then isopropanol before and after the laser processing procedure. To enhance absorption on the glass substrate, we opted to deposit a bilayer thin film system comprising Silver (Ag) and Chromium (Cr). It is widely accepted that Ag film exhibits excellent absorption properties, while the Cr layer serves to strengthen the adhesion of Ag onto the substrate. The choice of film thickness values for the bilayer system is more important for creating highly regular structures on dielectric substrates. Dostovalov et al. [28] reported LIPSS on chromium films with different thicknesses and observed that highly ordered structures are formed when the film thickness is less than 125 nm, while LIPSS on thicker films (>125 nm) is accompanied by the formation of poorly ordered ablation structures due to oxidation. Therefore, we have decided to perform this experiment using a bilayer thin metal film system (30 nm Cr + 100 nm Ag). The desired thicknesses of both Cr and Ag were deposited by direct current (DC) magnetron sputtering of a 4-inch Cr target and a 2-inch Ar one on a soda-lime glass substrate having thicknesses of ≥3 mm. The Cr layer was deposited prior to the Ag layer to enhance the adhesion of Ag onto the substrate. Both thin film deposition runs were performed at a pressure of 0.5 Pa with 20 sccm of Ar as a sputtering gas, while maintaining power at 200 W (Cr) and 50 W (Ag) during 36 s and 90 s respectively (substrate-target distance close to 10 cm). The HV chamber process is described in the previous report by Graillot-Vuillecot et al. [29], and the classical circular magnetrons in cold configuration have been used for Cr and Ag deposition [30]. This substrate was used for thin film-mediated-LIPSS formation on glass.

A linearly polarized Yb: YAG femtosecond pulsed laser system (Satsuma, Model, Amplitude) emits laser pulses characterized by their pulse duration (τ) of 300 fs, a center wavelength (λ) of 1030 nm (equivalent to a single photon energy of 1.20 eV), a maximum pulse

Table 1
Composition of the soda-lime glass measured by X-fluorescence [27].

Elementals	(%mol)
SiO_2	72
CaO	9.9
Al_2O_3	2.1
Na_2O	15.5
K_2O	0.3
CeO_2	0.1
Fe_2O_3	0.1

repetition rate (f) of 250 kHz, and a pulse energy (E) of up to 10 μJ. In this work, laser processing has been carried out in both static and dynamic (scanning) modes for top irradiation. A schematic representation of the experimental setup for fs-laser processing on soda-lime glass is given in Fig. 1. The laser beam was focused onto the sample surface by a spherical lens (75 mm). Double-sided copper tape has been used to attach the bottom side of the glass substrate to the sample holder. Furthermore, on the top of the glass surface, we used thin film as a metal layer for SPPs excitation. LIPSS were produced by irradiating the sample surface (both top and bottom irradiation) at normal incidence within an ambient air atmosphere. Different values of fs-laser repetition rate (f), laser fluence (F), and focal distance (f_d) were selected as the parameters for investigating the formation of LIPSS on soda-lime glass. We utilized linearly polarized laser pulses with a Gaussian beam spatial profile. The beam spot size and fluence were adjusted by the distance between the focal lens and the material surface. In the single spot case, the working distance (from the focusing lens to the substrate surface) was determined to be approximately 72 mm. A Gaussian beam profile (with $M^2 \sim 1.08$) and a beam diameter (at the lens) of about 2.5 mm were directed onto the sample surface to generate the LIPSS profile. For the top irradiation, the obtained beam diameter is 33 μm and the calculated focal depth is 1.72 mm. Nevertheless, the values undergo slight alterations attributed to the extended focal distance of 75 mm (3 mm substrate thickness) for bottom irradiation. Thus, the beam diameter and the focal depth are 35 μm and 1.8 mm, respectively. Therefore, the fluence values can be varied accordingly with the changes in beam diameter and focal length.

This study employed three characterization approaches. Firstly, we examined the laser-irradiated sample surfaces using a Zeiss Supra 40 scanning electron microscopy with a field emission gun (SEM - FEG). Before the SEM observation, the glass substrate experienced platinum sputtering (4 nm) in a Leica sputter coater to avoid the charging effect during the measurement. The SEM instrument with a secondary electron detector, operates at an accelerating voltage ranging from 1 kV to 5 kV. In each instance, the characterization was performed within the central region of the sample, and their chemical composition was determined using an energy dispersive X-ray spectroscopy (EDX) detector with an accelerated voltage of 10 kV. Secondly, the presence of LIPSS, their amplitude and periodicity were identified and measured using a Bruker Dimension Icon atomic force microscope (AFM). Finally, Laser-induced breakdown spectroscopy (LIBS) measurements were also conducted to provide evidence of the presence of Cu ions in the formation of LIPSS, followed by determining the heat accumulation caused by copper ions.

3. Results and discussion

3.1. Thin film-mediated LIPSS on glass (top material irradiation in static mode)

In this study, to induce absorption on the surface of soda-lime glass, we utilized high repetition rates of 10 kHz, 50 kHz, 100 kHz, and 250 kHz, each with a constant energy of 10 μJ. The number of laser pulses (N) applied onto the same area can significantly influence the dynamics, morphology, and periodicity of LIPSS formation [21]. In Fig. 2, SEM images illustrate the features of LIPSS depending on the repetition rates on soda-lime glass in the static mode, at a central wavelength of 1030 nm. We performed the laser texturing with a process time of 1 second for the entire range of repetition rates (10 to 250 kHz) which means ($N = 10^4$ to $25\ 10^4$). As the process period decreases versus the repetition rate, the post-irradiation cooling not allows to reach the initial (ambient) temperature leading to heat accumulation that is more significant in dieletric substrates as sodalime.

The average fluence of four different LIPSS formations is $F = \sim 2$ J/cm^2. In the case of $f = 10$ kHz, the low laser frequency leads to the formation of HSFL (Fig. 2a), parallel to the polarization (**E**) direction of the laser beam. According to reports, HSFL with small period sizes ($\lambda_{HSFL} < \lambda/2$) have been predominantly observed in transparent materials, with orientations frequently perpendicular and occasionally parallel to the polarization direction [19] due to self organization. The development of these smooth regions is a consequence of insufficient beam ablation [31]. The spatial period (Λ) of the observed irregular LIPSS is about 180 ($\pm$10) nm. Thus, increasing the *f* to 50 kHz results in the formation of the same HSFL structures which become more pronounced and regular, and the Λ size is slightly increased up to about 200 ($\pm$10) nm as given in Fig. 2b. A further increase of *f* to 100 kHz increase the area covered with LIPSS keeping the direction parallel to the **E**, resulting in a homogenous pattern of HSFL (Fig. 2c). The observed regular HSFL period is about 250 ($\pm$10) nm. At a high repetition rate (250 kHz), the alignment of highly regular HSFL is formed which is parallel to the polarization, **E**, and the Λ size is 275 ($\pm$10) nm (Fig. 2d). The repetition rate has influenced the period structures, sizes, and morphologies. At low *f*, the interaction between laser plasma and thin film significantly impacted smooth material irradiation, producing irregular period structures (Fig. 2a,b). On the other side, at high *f*, the laser-plasma interaction effectively removed the thin film layer during top material irradiation of the glass (see EDX results Fig. 2h), leading to the formation of highly regular period structures (Fig. 2c,d). The LIPSS generation is largely related to surface melting [32,33].

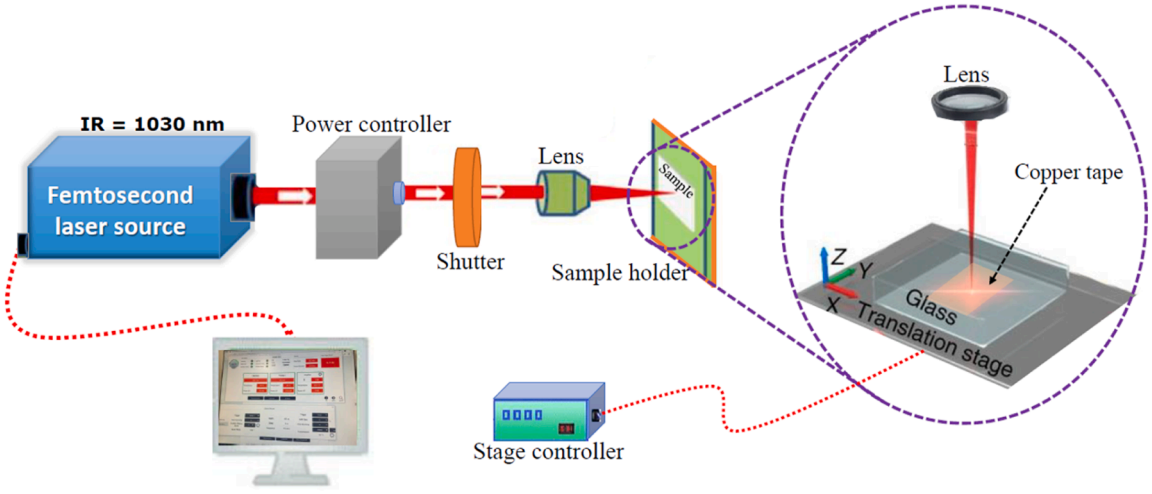

Fig. 1. Schematic of experimental setup process used for femtosecond (Yb:YAG) laser processing on soda-lime glass. Please note that this experiment is performed in two types: (1) with a bilayer metal thin film system (30 nm Cr + 100 nm Ag) for top irradiation, and (2) without a thin film system for bottom irradiation.

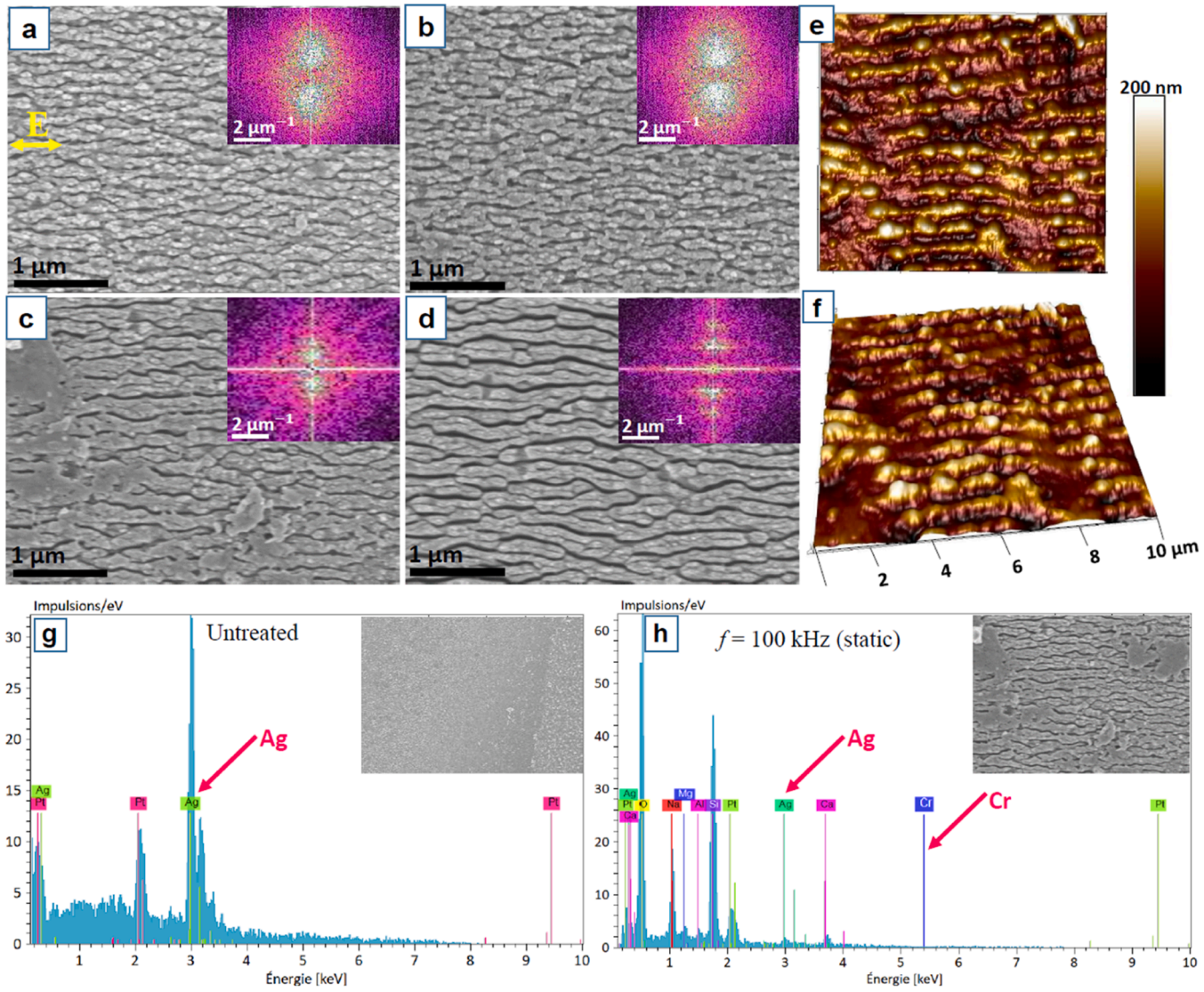

Fig. 2. (a-d) presents SEM images (top irradiation) depicting the surface of thin film-mediated LIPSS on soda-lime glass under irradiation with varying repetition rates: (a) 10 kHz, (b) 50 kHz, (c) 100 kHz, and (d) 250 kHz. The 2D FFT of the SEM images is displayed in the inset of each corresponding image. Fig. 2 (e and f) showcase the 2D and 3D AFM images of the HSFL at 100 kHz. Fig. 2 (g and h) displays the EDX spectrum capturing the surface composition of a thin film-mediated LIPSS on soda lime glass through top irradiation. Fig. 2(g) represents the untreated surface, and (h) showcases the LIPSS region at 100 kHz repetition rate. The inset images of Fig. 2 (g and h) represents the magnified views of both the untreated and HSFL images.

The 2D Fast Fourier Transform (2D-FFT) images of a large area reveal the periodicity of HSFL structures, as depicted in the insets of Fig. 2(a-d). The confirmation of LIPSS periodicity aligns with the SEM images. The inset Fig. 2(a) fails to define a periodic pattern at 10 kHz; but, it presents a mere depiction of the rough topology of HSFL at 50 kHz, which is given in inset Fig. 2(b). At 100 kHz, remarkably clear HSFL ripples are observed, confirmed by the marked defect lines in inset Fig. 2(c). The HSFL ripples exhibit a periodicity size of 250 (±20) nm parallel to the polarization direction. At 250 kHz, distinct HSFL ripples aligned direction parallel to **E** are visible in inset Fig. 2(d). The quantitative analysis of FFT data allows for the assessment of LIPSS periods, revealing a notably consistent quasi-constant periodicity of 275 (±20) nm in the prominent HSFL, complemented by SEM observations. The images in Fig. 2(e) and (f) represent 2D and 3D AFM visualizations, respectively, for the repetition rate of 100 kHz. In this scenario, the AFM-scanned zone (10 × 10 μm^2) reveals an HSFL period size of 260 (±20) nm, closely aligning with the SEM-FFT values for the respective material surface.

Furthermore, EDX analysis was employed to examine the chemical composition of the surfaces before and after the laser irradiation. Fig. 2 displays representative signals for the material surface exposed to the optimum repetition rate of 100 kHz, along with signals from the untreated film. In Fig. 2, SEM images corresponding to untreated (g) and 100 kHz frequency treated surface (h). The EDX spectra of the untreated sample (Fig. 2, g) revealed signals of silver (Ag), evidencing the sputtered Ag thin layer, and platinum (Pt) originating from the conductive thin film deposited for SEM measurement. After irradiation at 100 kHz (LIPSS regime), the material surface exhibits signals including Si, O, Na, Mg, Al, and Ca, originating from the soda-lime glass. Notably, Si and O demonstrate particularly strong signals compared to the other elements (Fig. 2, h), signifying their noticeable presence from the glass surface as evidenced in Table 1 (chemical composition of soda-lime). Furthermore, weak signals arise from Ag, and there is no signal from Cr, indicating their removal during laser irradiation and confirming their contributions to the generation of LIPSS on the glass substrate.

In summary, the irradiation of soda-lime glass in this configuration predominantly exhibits HSFL aligned parallel to the laser beam polarization. The observed periodicity ranges between 180 (±10) nm and 275

(±10) nm, showing a gradual increase with the rising repetition rate.

3.2. Thin film-mediated LIPSS on glass (top material irradiation in scanning mode)

In this section, dynamic scanning mode investigation is conducted to achieve uniform structuring with HSF-LIPSS for the selected repetition rate of 100 kHz. To generate HSFL across a wide area, the laser irradiation was examined along a single scan line parallel and perpendicular to the axis of laser beam polarization. To achieve this, the surface of the soda-lime glass substrate coated with thin film layer was irradiated in a scanning manner at 100 kHz. The scanning occurred at a speed of ~1 mm/s in both horizontal and vertical directions. The spot diameter was approximately 30 μm in both scanning directions, and Fig. 3 (a, b) displays the corresponding SEM images. The HSFL generated on the material surface was qualitatively analyzed, revealing a noticeable redeposition of nanoparticles during parallel scanning (∥ to the **E**) in Figure 3(a) compared to perpendicular scanning (⊥ to the **E**) in Figure 3 (b). Thus, it is evident that the alignment of the laser beam scanning axis with the polarization direction significantly affects the uniformity of large-area processing with higher redeposition. R. Rajendran et al. [34] observed similar behavior in the redeposition of nanoparticles on a borosilicate surface during large-area scanning at a speed of 1 mm/s.

LIPSS formation occurs parallel to the polarization in both scanning directions. However, vertical/perpendicular scanning displays highly regular HSFL periods compared to horizontal/parellel one. The 2D-FFT images displaying the large area periodicity of HSFL formation are presented in the insets of Fig. 3 (a, b). The quantitative analysis of the FFT data assesses the HSFL, indicating a periodicity of around 135 (±10) nm for perpendicular scanning and 115 (±10) nm for parallel scanning. Hence, Fig. 3 indicates that the preferable scan speed for generating regular periodicity LIPSS is 1 mm/s in the vertical scanning (⊥) when compared to horizontal scanning (∥) direction to the **E**.

The representative signals (EDX) for the material surface exposed to the optimum repetition rate $f = 100$ kHz at vertical scanning direction to the polarization as given in Fig. S1 (suplimentary materials). The LIPSS regime exhibits signals including Si, O, Na, Mg, Al, and Ca, originating from the soda lime glass. Additionally, Ag denotes a thin film layer, consistent with observations in static mode in Fig. 2(h). The presented table in Figure S1 indicates that the chemical composition of Si and O exhibits higher occupancy on the LIPSS surface, as evidenced by Table 1, thereby confirming the formation of HSFL on the soda-lime glass substrate.

3.3. Thin film-mediated LIPSS on glass (bottom material irradiation in static mode)

According to the literature, the laser fluence needs to be at a minimum of ~ 5 J/cm^2 and or the energy to reach about 20 μJ for the effective absorption of the laser beam on wide bandgap materials [25]. At minimum laser energy, the laser beam diffuses completely within the transparent glass substrate, preventing from absorption or texturing of its surface. Choosing a higher laser repetition rate presents a favorable solution to resolving absorption issues on dielectric materials.

Considering the results outlined above in Section 3.1, the glass substrate coated with a thin film was employed on the opposite side for laser irradiation (bottom/or back side irradiation), as illustrated clearly in the photo/images presented in Fig. S2 (supplementary materials). In this experiment, copper (Cu) tape was utilized and positioned between the substrate and sample holder to secure the substrate in place. For this analysis, we utilized a consistent energy of 10 μJ across a range of repetition rates, spanning from 10 kHz to 250 kHz for 1 second time duration, as detailed in Section 3.1. Across all repetition rate cases, there was no absorption nor texturing on the top surface of the glass, as the laser beam fully diffused inside the transparent glass substrate, interacting solely with the thin film coated on the bottom side.

Fig. 4 (a-d) provides a comprehensive view of the SEM micrographs depicting the formation of LIPSS at different repetition rates ranging from 10 kHz to 250 kHz, respectively. The average spot diameter was 35 μm, with slight variations occurring for each repetition rate, consequently leading to a slight change in laser fluence, ranging from ~ 1.75 J/cm^2 to ~ 2 J/cm^2. Regular formation of LIPSS was observed at 10 kHz, as depicted in Fig. 4(a), with the HSFL direction parallel to the **E**. Simultaneously, significant redeposition of nanoparticles took place on the surface of the HSFL. The specific value of Λ_{HSFL} depends on the respective repetition rate, which is correlated with the energy distribution of the fs-laser beam. At 10 kHz, the measured spatial period value is $\Lambda_{HSFL} = 200$ (±10) nm. The increase of $f = 50$ kHz yields a highly regular formation of parallel HSFL in the central region of the irradiated area with the absence of redeposition. This increase leads to a larger periodicity of $\Lambda_{HSFL} = 310$ (±10) nm, as shown in Fig. 4(b). A subsequent increase in $f = 100$ kHz induces a modification in LIPSS orientation from parallel to perpendicular to the laser beam polarization, **E**, illustrated in Fig. 4(c). Hence, it is clear that the alignment of LIPSS is significantly affected by the repetition rate during bottom irradiation. This could be attributed to the change of energy distribution across the ablated area caused by the coupling of metal and the thin film-coated glass substrate. This transition from HSFL to LSFL formation results in an increased periodicity of $\Lambda_{LSFL} = 510$ (±15) nm, demonstrated in Fig. 4(c). The distribution of LSFL persists with a further increase of the repetition rate up to 250 kHz, resulting in an enlarged period size of 550

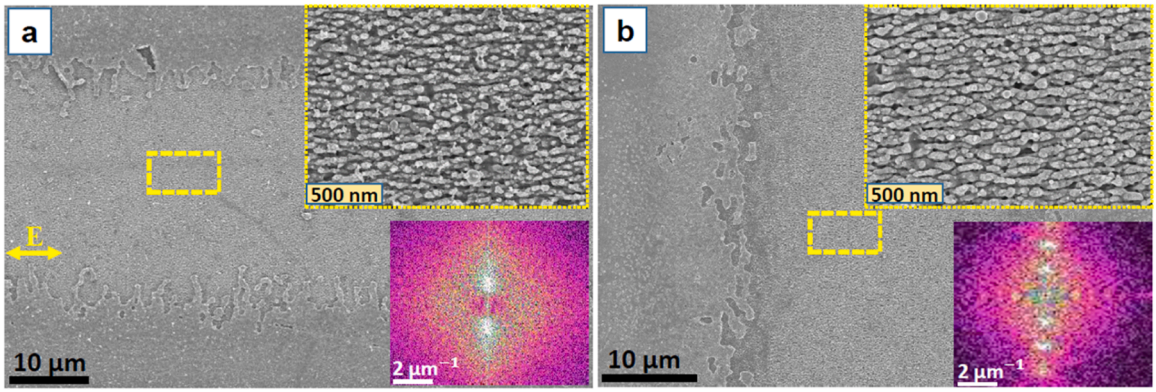

Fig. 3. (a, b) SEM images (top irradiation) of the surface of thin film mediated LIPSS on soda lime glass with a scanning speed (SS) of ~1 mm/s along horizontal (a) and vertical (b) direction with the laser repetition rate is 100 kHz. The magnified image of HSFL and the 2D FFT of the SEM image are shown in the inset of each images.

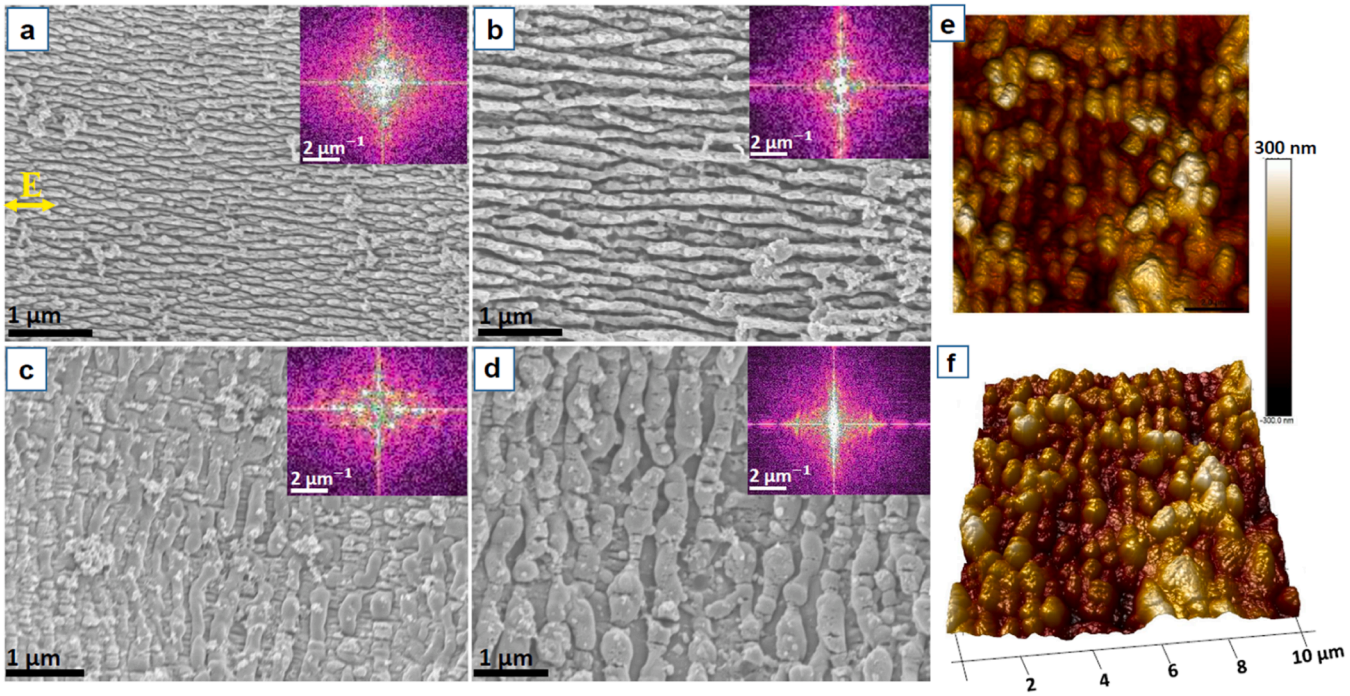

Fig. 4. (a-d) SEM images (bottom irradiation) of the surface of thin film-mediated LIPSS on soda-lime glass under irradiation with varying repetition rates: (a) 10 kHz, (b) 50 kHz, (c) 100 kHz, and (d) 250 kHz. The 2D FFT of the SEM images is displayed in the inset of each corresponding image. Fig. 4(e and f) showcase the 2D and 3D AFM images of the LSFL at 100 kHz.

(±10) nm (Fig. 4, d). However, partial redeposition of nanoparticles persists over the LIPSS in both LSFL cases, underscoring the significant role of metal (Cu) ions in this redeposition process. It can be concluded that the repetition rate is the primary factor influencing the preservation of the LIPSS arrangement for both HSFL (∥ to the **E**) and LSFL (⊥ to the **E**). Xuesong Shi et al. [35] reported that the transition from HSFL to LSFL occurs with increasing fluence values on a fused silica substrate. Other reports have also found that the transition from HSFL to LSFL occurs as the fluence [21,36] is increased.

2D-FFT representations were displayed in the insets of Fig. 4(a-d), which confirms the consistency of LIPSS periodicity. In Fig. 4(a) inset, only the rough topology of HSFL was observed at 10 kHz. Upon increasing the repetition rate to 50 kHz, a clear observation of HSFL ripple alignment was evidenced in inset Fig. 4(b), marked by periodic lines, similar to the SEM observation. For 100 kHz, the LIPSS periodicity transitioned from HSFL to LSFL, with the period size increases from 300 (±10) nm to 500 (±10) nm, respectively (inset Fig. 4b and c). The LSFL ripples align direction perpendicular to the **E**. At 250 kHz, large LSFL ripples associated direction perpendicular to the **E** are noticeable in inset Fig. 4(d). The observed LSFL ripples exhibit a quasi-constant periodicity of 550 (±10) nm. Fig. 4(e) and (f) display 2D and 3D AFM visualizations, respectively, for the repetition rate of 100 kHz. In this context, clear LIPSS periods were observed in both the 2D and 3D images. The scanned area (10 × 10 μm^2) revealed an LSFL period size of 500 (±25) nm, closely aligning with the SEM-FFT values obtained for the material surface.

Figure S3 (supplementary materials) shows the EDX spectrum of the soda-lime glass substrate for untreated surface (a), under 100 kHz irradiation (b), and the border zone (near the LIPSS regime) are depicted in (c). The EDX spectra of the untreated sample (Figure S3, a) exhibited only signals for Ag and Pt, consistent with those observed in Fig. 2(g). When subjected to 100 kHz irradiation (LIPSS regime), the material surface displays signals such as Si, O, Na, Mg, Al, and Ca, originating from the soda-lime glass. Moreover, Figure S3 (b) highlights the remarkable strength of Si and O signals in comparison to the other elements, as evidenced in Table 1. Additionally, the presence of copper (Cu) signal also emerges from the LIPSS regime. This is because both Cu and the thin film were simultaneously involved during laser irradiation. Subsequently, Cu ions from the irradiated area diffused onto the glass substrate due to plasma formation (coupling between the surface electrons and the incident electric field), thereby supporting the contribution to the formation of LIPSS on glass substrate. Furthermore, our observation highlights the significant role of Cu metal in transitioning the spatial period of LIPSS from HSFL to LSFL, evident through its higher signal compared to Ag (also confirmed in the table by considering the limitations of EDX accuracy). Figure S3 (c) specifically highlights the border regime observed near the LIPSS, displaying a notably stronger Cu signal than Ag.

Several reports have explained the relationship between energy density (fluence), and the number of pulses with LIPSS periodicity, whereas the impact of repetition rate significantly influences the formation of periodic structures [37]. The LIPSS spatial period as a function of repetition rate is depicted in Fig. 5 for both types of irradiations (top and bottom). The figure illustrates that the spatial periods for top irradiation, exhibit an increase from 180 (±10) nm to 275 (±10) nm as the repetition rate is increased from 10 kHz to 250 kHz, respectively. The increasing trend of HSFL spatial periods is attributed to chemical expansion, and or high energy accumulation in the ablation regime. For bottom irradiation, the observed periodicity of HSFL remains the same until 50 kHz, beyond which it transitions to LSFL at high repetition rates (100 kHz, 250 kHz). As the pulse number increases by *f*, the surface morphology undergoes a possible transition process from HSFL to LSFL. The results indicated that HSFL and LSFL transformation occurs from the electromagnetic mechanism involving local field enhancement and field interference during multi-pulse irradiation [38]. The observed LSFL spatial period ranges from 510 (±10) nm to 550 (±10) nm for 100 kHz and 250 kHz, respectively. This confirms that the effective number of pulses strongly influences the spatial periods.

3.4. Direct LIPSS on glass (bottom material irradiation in static mode)

In this study, we aim to explore the impact of the focal distance

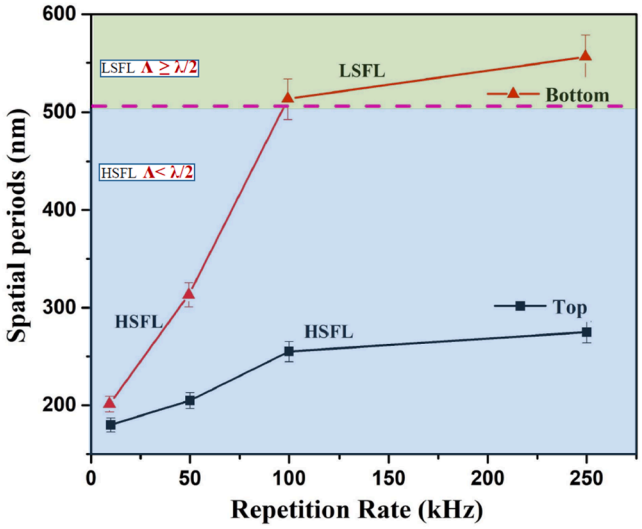

Fig. 5. Spatial period of parallel ($\Lambda_{HSFL}\parallel$) and perpendicular ($\Lambda_{LSFL}\perp$) LIPSS as a function of repetition rate under static mode for bottom and top irradiations in the case of thin film-mediated LIPSS.

between the lens and the substrate for the formation of LIPSS on a soda lime-glass substrate. The generation of LIPSS was observed on the substrate bottom surface when employing a maximum repetition rate f = 250 kHz, a pulse count of $N = 250 \times 10^3$, and an energy of 10 μJ. Generally, In dielectric materials, the anticipated period (Λ_{LSFL}) is expected to align direction perpendicular to the **E**, although occasionally, they may also align parallel to it [19]. It has been proven that both LSFL and HSFL can be obtained on dielectric or wide bandgap materials, especially on fused silica [25,36,39]. Accordance with the literatures, LIPSS initiation occurs at the boundary of the laser-irradiated spot when reaching a threshold laser fluence, and then they expand to cover the entire area. In general, at low laser energy, LSFL tends to appear on the outer boundary of the spot, whereas HSFL is noticed on the inside. As the laser energy increases, it allows LSFL to occupy the entire ablated area. Multiple researchers have documented this transition across various materials. This phenomenon has been validated through several dielectric materials, including fused silica, borosilicate, and soda-lime silicate [25].

Fig. 6 (a, b) displays SEM images depicting the LIPSS formed on the glass substrate surface, captured at two distinct focal distances: 71 mm and 72 mm, respectively. At a focal distance of 71 mm, we observed LSFL formation with a period size of 540 (±10) nm with a direction perpendicular to the **E** depicted in Fig. 6(a). The uniform occurrence of LSFL indicates the dispersion of laser energy throughout the entire ablated zone. At a focal distance of 72 mm, we observed consistent LSFL with a direction perpendicular to the **E** (Fig. 6b). Simultaneously, the period size of the LSFL increased to 585 (±10) nm. Bonse et al. [19] observed that the period size of LSFL measures approximately 500 nm when utilizing a laser wavelength of 800 nm on a fused silica substrate. This observation likely contributes to our understanding of the behavior and characteristics of LSFL on such substrates. It is worth noting that the periodicity of LSFL increases with increasing focal distance between lens and the substrate. In Fig. 6(c), the 3D AFM image (10 × 10 μm^2) represents the optimal focal distance of 72 mm. It distinctly exhibits LSFL periods, similar to the SEM image depicted in Figure 6(b). Fig. 6 (d and e) display the EDX spectra for the soda-lime glass substrate surface in its untreated regime and under 250 kHz irradiation (LIPSS regime), respectively. The EDX spectra of the untreated sample (Fig. 6, d) exhibited the predicted signals, including Si, O, Na, Mg, Al, and Ca, originating from the glass material. While, the LIPSS regime (Fig. 6, e)

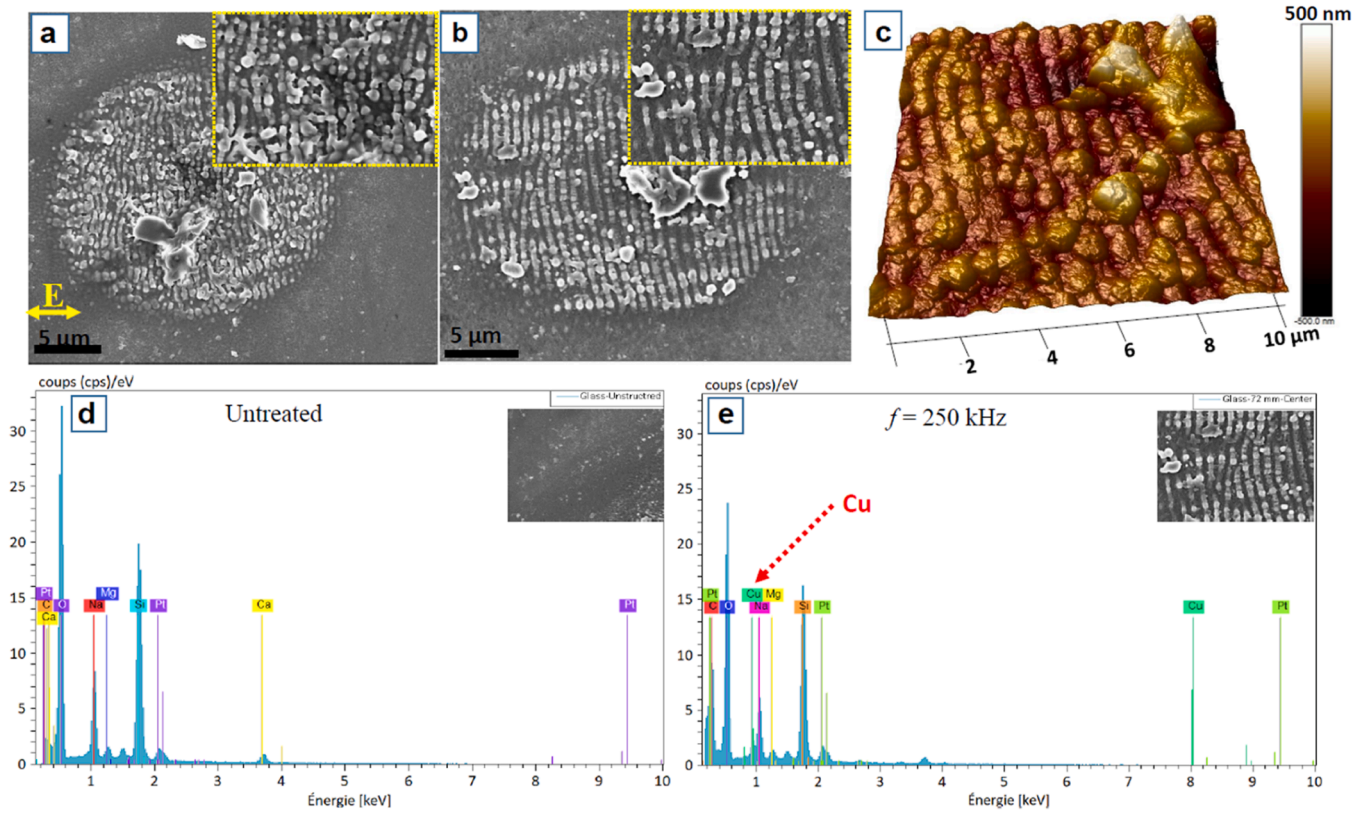

Fig. 6. (a, b) SEM images of soda-lime glass substrate after the exposure at 250 kHz ($N = 250 \times 10^3$ pulses) at different focal distances: (a) 71 mm and (b) 72 mm, (c) represents the 3D-AFM image at 72 mm. Fig. 6(a-c) showcase the images representing LSFL. Fig. 6(d and e) represents EDX spectra of the untreated surface, and LIPSS region at 100 kHz repetition rate, respectivey. The inset images of figure (d and e) represents the magnified views of both the untreated and HSFL images.

has revealed a signal from Cu, suggesting its significant contribution to the formation of LIPSS on the glass substrate. As outlined in Section 3.3, Cu metal significantly contributes to the formation of LSFL at a high repetition rate (250 kHz).

So far, LIPSS formation on soda-lime glass has been investigated by Stephan Gräf et al. [25] using a femtosecond laser operating at a fluence of 4.1 J/cm^2 and a repetition rate of 1 kHz, employing a single spot irradiation technique. However, they observed rare occurrences of melted LSFL across the entire spot area, primarily attributed to significant surface melt formation. In our study, we observed the formation of regular LIPSS at a fluence of ~ 2.5 J/cm^2 and the repetition rate of 250 kHz, in both cases of two distinct focal distances.

Our findings will aid in tailoring LIPSS-based structures on soda-lime glass, especially significant for high repetition rates. These advancements hold particular promise to intricate applications in plasmonics [40], manipulating cell behavior via patterned surfaces [41,42], microfluidic devices [43], and crafting surfaces with targeted wetting properties [44,45].

3.5. Mechanism of direct and thin film-mediated LIPSS formation on soda lime glass

Indeed, the literature offers various perspectives on the proposed mechanisms underlying LIPSS formation on dielectric materials. According to the Sipe theory, the formation of LIPSS on dielectric materials is attributed to radiation remnants (RR) [46]. Here, we explore possible mechanisms for both LSFL and HSFL formation on soda-lime glass, providing an in-depth examination of these mechanisms under various conditions. Fig. 7 provides a schematic representation illustrating these mechanisms across three different scenarios.

(i) Figure 7(a) describes thin film-mediated LIPSS on soda-lime glass (top material irradiation; Section 3.1), this involves the interference between incident light and the electromagnetic wave of the thin film (Ag+Cr) layer by SPPs. Here, thin film layer plays a key role in absorbing light into the conduction band of the metal film, exciting electrons to the valence band through multi-photon absorption. This demonstrates a shared aspect in the formation of LIPSS on metals or semiconductors, induced by SPPs on a glass substrate through thin film absorption. As the repetition rate increases, the metal film layer is subsequently removed by a higher number of pulses, resulting in the formation of high spatial LIPSS on the glass substrate. This phenomenon, known as HSFL, can be attributed to potential factors such as self-organization [15] or the involvement of distinct plasmon modes [47].

(ii) Figure 7(b) defines thin film-mediated LIPSS on soda-lime glass (bottom material irradiation; Section 3.3). Under these circumstances, we utilized copper tape to affix the substrate onto the sample holder, as outlined in Figure S2 (supplementary materials). The distinct formation of LIPSS on the bottom side is notably different due to the important function of the copper tape during the irradiation process on the glass substrate. In this context, the incident laser beam initially diffuses within the glass substrate, facilitating interaction with the copper tape along with the metal film to induce SPPs interference, resulting in the generation of LIPSS on the glass material. At high repetition rates (100 kHz and 250 kHz), bottom irradiation exhibited LSFL with 510–550 (±10) nm spatial periods direction perpendicular to the laser beam polarization. LSFL can emerge through a process involving local melting and a rapid solidification process. While the excitation of a scattered electromagnetic wave from the rough surface (thin film) of the material and copper tape contributes to this type of LSFL formation.

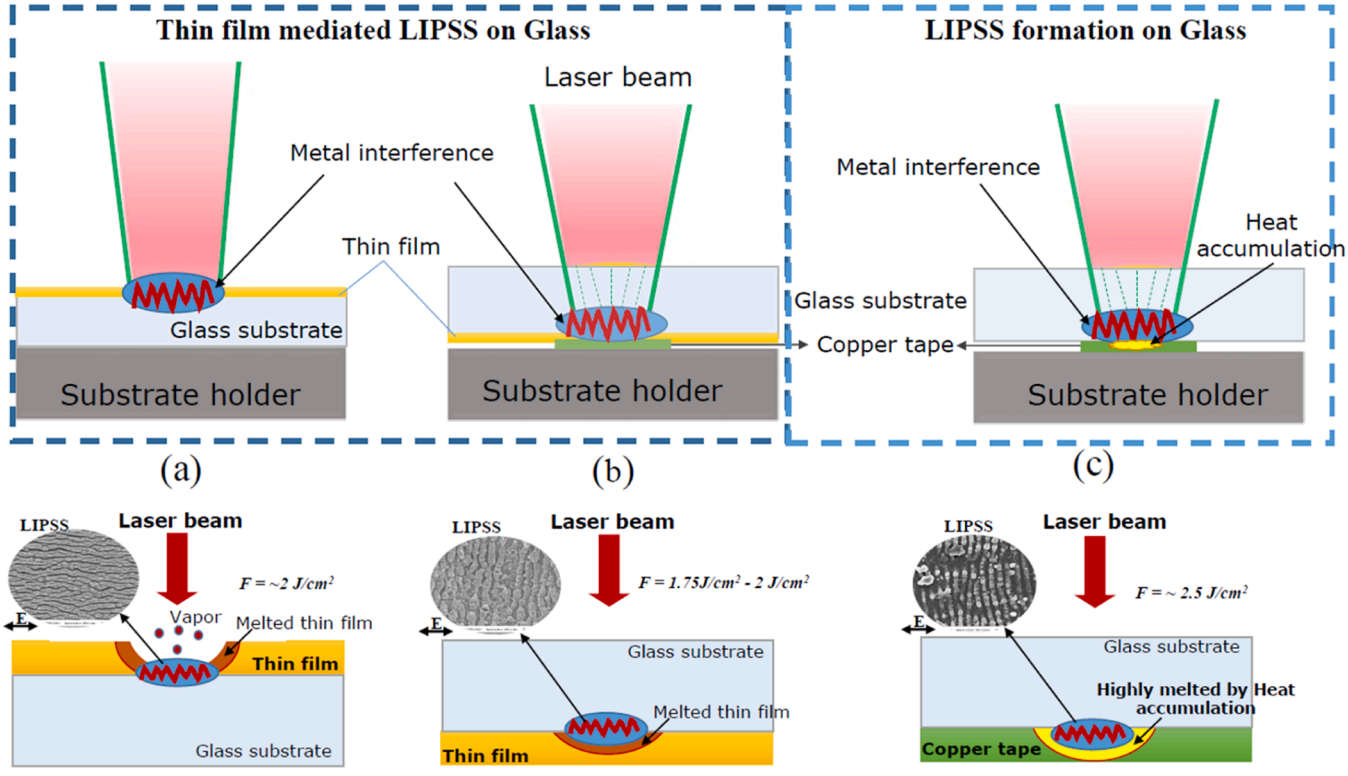

Fig. 7. A schematic representation outlining the potential mechanisms for LIPSS formation: (a) For the top irradiation, the electromagnetic wave of the thin film (Ag+Cr) layer which primarily driven by the SPPs. (b) For the bottom irradiation, laser beam initially diffuses within the glass substrate, followed by the interaction between copper tape and metal film creates SPPs interference. (c) For the bottom irradiation without thin film layer, the diffused laser beam which enabling interaction only with copper ions to creates SPPs interference by substantial accumulation (heat accumulation) of plasma ejection from the copper ions.

(iii) Fig. 7(c) defines LIPSS generation on soda-lime glass (bottom material irradiation; Section 3.4). This investigation utilized the optimal repetition rate of 250 kHz. Referring to the prior instance in Figure 7(b), the same mechanism takes place as the incident laser beam initially diffuses within the glass substrate, enabling the coupling of copper ions to induce SPPs typically involves the interaction of copper ions with substrate surface, leading to the generation of LIPSS on the glass material. The process occurs due to the substantial accumulation (heat accumulation) of plasma ejection from the copper surface (detailed discussion is presented in Section 3.6). However, the spatial period size increases up to 585 (±10) nm when compared to the thin film-mediated LIPSS (550 (±10) nm) with the same *f*. The findings highlight a noteworthy change in the spatial period when transitioning between thin film-mediated and direct laser irradiation.

3.6. Laser-induced breakdown spectroscopy (LIBS)

Identifying copper (Cu) within the meterial is crucial to confirm the presence of heat accumulation during laser irradiation, essential for the formation of LIPSS. Spectroscopic analysis was conducted through LIBS investigation, utilizing an optical multi-channel analyzer. In Fig. 8, the emission spectrum of neutral copper (Cu I) displays wavelengths at 327 nm, 512 nm, and 520 nm, obtained from copper tape along with glass substrate. Additionally, the broader ionic line of Cu II emerges around the wavelength range of 600 nm −700 nm. These findings suggested that the plasma induced a higher concentration of atomic Cu within the copper tape compared to ionic Cu, facilitated by the femtosecond laser. Moreover, the presence of nitrogen (N_2) is a typical occurrence in the atmosphere and is associated with the copper surface. The emission spectrum validates that the current LIBS method is capable of identifying the presence of Cu ions. The detailed experimental procedures and results have been discussed in the supplementary materials.

3.6.1. Heat accumulation (effect of repetition rate)

Performing laser irradiation with a continuous stream of pulses at high repetition rates, insufficient time for complete cooling of the material causes a rise in the base material temperature [48]. This phenomenon referred to as the heat accumulation process. In order to estimate the heat accumulation during the multipulse laser treatment of glass substrate, it is essential to assess when the surface reaches its maximum heating temperature at one end and starts cooling with respect to the laser pulses. In this scenario, we assume that the absorbed laser energy is utilized for heating, and the cooling process initiates as soon as the maximum heating temperature is attained. The substrate temperature distribution can be estimated using the following relation [49];

$$T_{\max} = \frac{\alpha A E}{C} \tag{1}$$

$$T_{\max} = \frac{\alpha A E - \rho L}{C} \tag{2}$$

where, $T_{\max}$ is the maximum temperature, E is the laser fluence, A is the absorptivity, and C denotes the volumetric heat capacity of the glass substrate. Eq. (2) denotes the realistic maximum temperature which include the Enthalpy of melting (L_m) along with the density (ρ). During laser treatment at a high repetition rate, the glass substrate's surface might not sufficiently cool to its initial temperature between pulses. Consequently, the residual temperature of the surface after the impact of a number of pulses (N) when the $N+1$ th pulse arrives can be assessed using the following relation [49];

$$\Delta T\left(t=\frac{N}{f}, r\right) = T_{\max}\sum_{i=1}^{N}\frac{r_0^2}{(r_0^2+4ai/f)}\exp\left(-\frac{r^2}{(r_0^2+4ai/f)}\right) \tag{3}$$

here, ΔT is the residual temperature, a is the thermal diffusivity, f is the pulse repetition rate, r_0 is the radius of the laser beam spot and r is the radial distance from the centre of the beam. This is crucial due to the fact that the dynamics of surface temperature are depending upon the number of laser pulses, N. The residual temperature ΔT serves as the initial temperature for the subsequent pulse and is influenced by the repetition rate, f. Simultaneously, the residual temperature remains independent of the pulse duration, allowing this expression to be employed for estimating the accumulated heat on the glass substrate surface when using ultrashort laser pulses. The calculations utilize parameter values for the glass substrate (dielectric material), which have been averaged from various literature sources [27,49-51]; α = 4800 cm^{-1}; A = 0.22 - 1; C = 1.78 $Jcm^{-3}.K^{-1}$; a = 0.034 - 0.063 $cm^2 s^{-1}$. Here, the effective absorption coefficient of soda-lime glass at the wavelength of λ = 10.6 μm is considered based on our prior study, as the same material is being used [27]. Fig. 9 displays the calculated temperature variation (at r = 0 μm) as a function of pulse number at different repetition rates of 10, 50, 100, and 250 kHz. As per Eq. (1), the

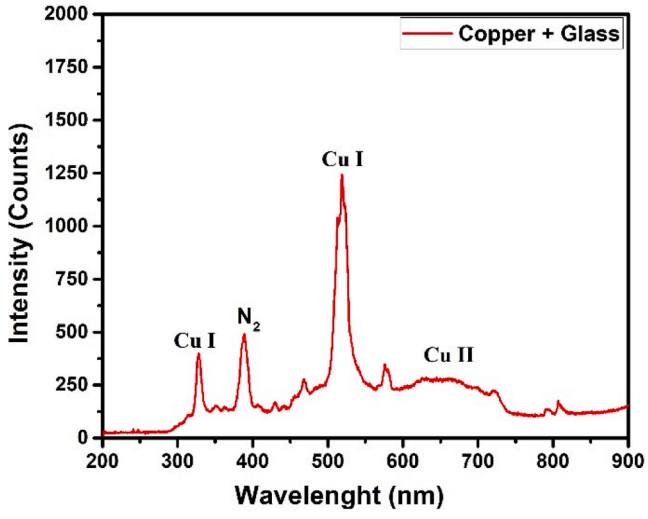

Fig. 8. Plasma spectrum of high purity copper tape with glass substrate during the laser irradiation with 1030 nm.

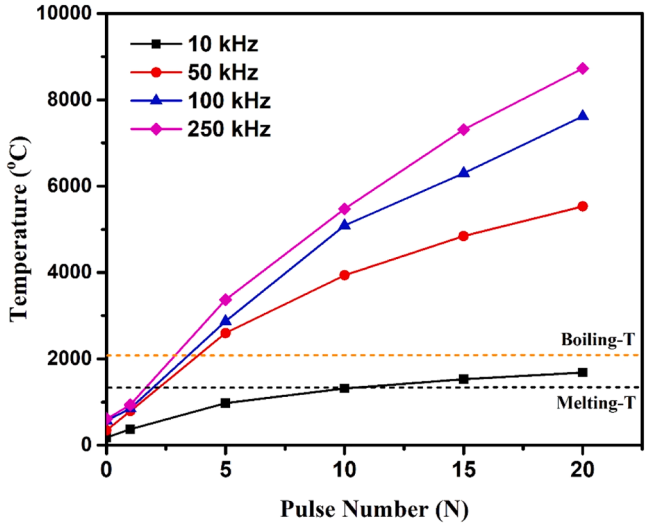

Fig. 9. The evolution of the calculated temperature with respect to the pulse number at various repetition rates, at a radial position of (r = 0 μm) from the center of the laser beam. The dashed lines indicates the melting and boiling temperatures.

maximum temperature (T_{max}) reaches approximately 965 °C (1240 K), falling within the temperature range between the transition (<600 °C) and melting (>1600 °C) temperatures of the glass substrate. However, when the Enthalpy of melting ($L_m = 100$ kJ/kg) is included along with the density ($\rho = 2520$ kg/m^3) for soda-lime glass, the absolute T_{max} was reduced to 800 °C using Eq. (2). The attained T_{max} is referred to as the operating temperature for the heat accumulation process. For the direct-LIPSS formation process, the initial temperature of heat accumulation on the soda-lime glass surface is ~925 °C after one pulse ($N = 1$), as determined by Eq. (3). This temperature increases to ~4120 °C after five pulses ($N = 5$) when irradiated with a femtosecond laser at a pulse repetition rate of 250 kHz. Shane M. Eaton et al. [52] observed a similar temperature enhancement, increasing from 1200 °C ($N = 1$) to 4200 °C ($N = 5$), for a borosilicate substrate when irradiated with a femtosecond laser at a pulse repetition rate of 500 kHz. Further increasing the number of pulses, the accumulated heat temperature also increases accordingly until it reaches the saturation temperature. This observation confirms that heat accumulation is strongly dependent on the number of pulses. As we used minimum energy with high repetition rates, the ablation temperature is achieved in a significantly shorter time duration. Consequently, the saturation temperature calculated using adiabatic Eq. (3) may not accurately represent the actual temperature range. Nevertheless, the approximate saturation temperature is reached to ~ 5200 °C within a 1 s duration for 10 kHz due to the higher number of pulses ($N = 10 \times 10^3$). The supplementary materials include a plot of the saturation temperature as a function of the number of pulses (Figure S6). On the other side, the obtained heat accumulation temperatures are 973 °C, 2600 °C, 3370 °C, and 4350 °C for different repetition rates, such as 10 kHz, 50 kHz, 100 kHz, and 250 kHz in the case of thin film-mediated LIPSS at $N = 5$. Hence, we can infer that significant heat accumulation occurs, leading to an expanding melted volume correlated with both pulse number and repetition rate.

4. Conclusions

We investigated the generation of both high-spatial-LIPSS (HSFL) and low-spatial-LIPSS (LSFL) on soda-lime glass using a femtosecond laser irradiation. Extensive studies were carried out to examine the influence of laser repetition rate and scan direction with laser polarization on large-area surface structuring. Thin film-mediated LIPSS for top material irradiation exposed HSFL for four different repetition rates from 10 kHz to 250 kHz with a time of 1 second, adjusting the number of pulses according to the each repetition rate. In contrast to the bottom irradiation, both HSFL at low frequencies (10 kHz, 50 kHz) and LSFL at high frequencies (100 kHz, 250 kHz), were observed and extensively discussed. Elemental analysis (EDX) confirms strong signals originating from Si and O, indicative the glass substrate; while detecting the least signals attributed to the thin film of Ag and Cr. In the case of direct LIPSS observation, no HSFL was detected. Instead, LSFL displayed with larger spatial periods, measuring 585 (±10) nm direction perpendicular to the **E**. Additionally, the EDX analysis confirms that the signals of Si and O originate from the spatial periods, with an additional observation of a Cu signal. This confirms the formation of LIPSS patterns on soda-lime glass material through laser-plasma interaction with the copper tap (Cu ions). In conclusion, the morphology of LIPSS on soda-lime glass shows two different forms: LSFL perpendicular to laser polarization and HSFL parallel to laser polarization.

CRediT authorship contribution statement

K. Deva Arun Kumar: Writing – original draft, Methodology, Investigation, Data curation, Conceptualization. **Alex Capelle:** Validation, Formal analysis, Data curation. **Wael Karim:** Investigation, Data curation. **Herve Rabat:** Visualization, Methodology, Formal analysis, Data curation. **Loic Gimenez:** Resources, Methodology, Data curation. **Barthélemy Aspe:** Writing – review & editing, Validation. **Amaël Caillard:** Writing – review & editing, Methodology, Investigation, Data curation. **Martin Depardieu:** Validation, Methodology, Investigation. **Anne-Lise Thomann:** Writing – review & editing, Methodology, Data curation, Conceptualization. **Nadjib Semmar:** Writing – review & editing, Validation, Supervision, Project administration, Methodology, Funding acquisition, Conceptualization.

Declaration of competing interest

The authors declare that they have no known competing financial interests or personal relationships that could have appeared to influence the work reported in this paper.

Data availability

Data will be made available on request.

Acknowledgment

The authors are grateful for the financial support from the Région Centre-Val de Loire in the framework of the ARD MATEX-SAILOR project. We would like to extend our sincere gratitude to S. Desprez for providing the glass samples and the CERTeM 2020 Program for supporting the cleanroom facilities.

Supplementary materials

Supplementary material associated with this article can be found, in the online version, at doi:10.1016/j.optlaseng.2024.108321.

References

[1] Maeder T. Review of Bi2O3 based glasses for electronics and related applications. Int Mater Rev 2013;58:3–40.
[2] Kilinc E, Hand RJ. Mechanical properties of soda-lime-silica glasses with varying alkaline earth contents. J Non Cryst Solids 2015;429:190–7.
[3] Hodgson SD, Waugh DG, Gillett A, Lawrence J. High speed CO2 laser surface modification of iron/cobalt co-doped boro aluminosilicate glass and the impact on surface roughness, gloss and wettability. Laser Phys Lett 2016;13:076102.
[4] Ruffino F, Grimaldi MG. Nanostructuration of thin metal films by pulsed laser irradiations: a review. Nanomaterials 2019;9(8):1133.
[5] Ahmmed K, Grambow C, Kietzig A-M. Fabrication of micro/nano structures on metals by femtosecond laser micromachining. Micromachines (Basel) 2014;5(4):1219–53.
[6] Vorobyev AY, Guo C. Direct femtosecond laser surface nano/microstructuring and its applications. Laser Photon Rev 2012;7(3):385–407.
[7] Breitling D, Ruf A, Dausinger F. Fundamental aspects in machining of metals with short and ultrashort laser pulses. In: Herman PR, Fieret J, Pique A, Okada T, Bachmann FG, Hoving W, Washio K, Xu X, Dubowski JJ, Geohegan DB, Traeger F, editors. SPIE proceedings. SPIE; 2004.
[8] Shimotsuma Y, Kazansky PG, Qiu JR, Hirao K. Self-organized nanogratings in glass irradiated by ultrashort light pulses. Phys Rev Lett 2003;91:247405.
[9] Phillips KC, Gandhi HH, Mazur E, Sundaram SK. Ultrafast laser processing of materials: a review. Adv Opt Photon 2015;7:684–712.
[10] Muller FA, Kunz C, Graf S. Bio-inspired functional surfaces based on laser-induced periodic surface structures. Materials (Basel) 2016;9:476.
[11] Birnbaum M. Semiconductor surface damage produced by ruby lasers. J Appl Phys 1965;36:3688–9.
[12] Bizi-Bandoki P, Benayoun S, Valette S, et al. Modifications of roughness and wettability properties of metals induced by femtosecond laser treatment. Appl Surf Sci 2011;257:5213–8.
[13] Dusser B, Sagan Z, Soder H, Faure N, Colombier JP, Jourlin M, Audouard E. Controlled nanostructrures formation by ultra fast laser pulses for color marking. Opt Express 2010;18:2913–23.
[14] Vorobyev AY, Makin VS, Guo C. Periodic ordering of random surface nanostructures induced by femtosecond laser pulses on metals. J Appl Phys 2007;101:034903. -1–034903-4.
[15] Reif J, Costache F, Henyk M, Pandelov SV. Ripples revisited: non-classical morphology at the bottom of femtosecond laser ablation craters in transparent dielectrics. Appl Surf Sci 2002;197–198:891–5.
[16] Rohloff M, Das SK, Hohm S, Grunwald R, Rosenfeld A, Krüger J, Bonse J. Formation of laser-induced periodic surface structures on fused silica upon multiple cross-polarized double-femtosecond-laserpulse irradiation sequences. J Appl Phys 2011;110:014910. -1–014910-4.

[17] Sipe JE, Young JF, Preston JS, van Driel HM. Laser-induced periodic surface structure. I. Theory. Phys Rev B 1983;27:1141–54.
[18] Dufft D, Rosenfeld A, Das SK, Grunwald R, Bonse J. Femtosecond laser-induced periodic surface structures revisited: a comparative study on ZnO. J Appl Phys 2009;105:034908. -1–034908-9.
[19] Bonse J, Krüger J, Höhm S, Rosenfeld A. Femtosecond laser-induced periodic surface structures. J Laser Appl 2012;24:042006.
[20] Chakravarty U, Ganeev RA, Naik PA, Chakera JA, Babu M, Gupta PD. Nano-ripple formation on different band-gap semiconductor surfaces using femtosecond pulses. J Appl Phys 2011;109:084347.
[21] Höhm S, Rosenfeld A, Krüger J, Bonse J. Femtosecond laser-induced periodic surface structures on silica. J Appl Phys 2012;112:014901.
[22] Rohloff M, Das SK, Höhm S, Grunwald R, Rosenfeld A, Krüger J, Bonse J. Formation of laser-induced periodic surface structures on fused silica upon multiple cross-polarized double-femtosecond-laser-pulse irradiation sequences. J Appl Phys 2011;110:014910.
[23] Rosenfeld A, Rohloff M, Höhm S, Krüger J, Bonse J. Formation of laser-induced periodic surface structures on fused silica upon multiple parallel polarized double-femtosecond-laser-pulse irradiation sequences. Appl Surf Sci 2012;258(23):9233–6.
[24] Sun Q, Liang F, Vallée R, Chin SL. Nanograting formation on the surface of silica glass by scanning focused femtosecond laser pulses. Opt Lett 2008;33:2713–5.
[25] Gräf S, Kunz C, Müller FA. Formation and properties of laser-induced periodic surface structures on different glasses. Materials (Basel) 2017;10:933.
[26] Sládek J, Hlinomaz K, Mirza I, Levy Y, Derrien T, Cimrman M, Nagisetty SS, Čermák J, Stuchlíková The Ha, Stuchlík J. Bulgakova highly regular LIPSS on thin molybdenum films: optimization and generic criteria. Materials (Basel) 2023;16:2883 (1-12).
[27] Capelle A, Aspe B, Shavdina O, Diallo B, Pellerin N, Depardieu M, Thomann AA-L, Semmar N. Study of CO2 laser-induced thermal stress mechanisms on decorative sodaoda-lime glass. J Laser Micro/Nanoeng 2023;18(3).
[28] Dostovalov AV, Korolkov VP, Okotrub KA, Bronnikov KA, Babin SA. Oxide composition and period variation of thermochemical LIPSS on chromium films with different thickness. Opt Express 2018;26(6):7712.
[29] Graillot-Vuillecot R, Thomann A-L, Lecas T, Cachoncinlle C, Millon E, Caillard A. Properties of Ti-oxide thin films grown in reactive magnetron sputtering with self-heating target. Vacuum 2022;197:110813.
[30] Sagara R, Kawamura M, Kiba T, Abe Y, Kim KH. Characteristics of Ag thin films sputter deposited using Ar or Kr gas under different pressure. Surf Coat Technol 2020;388(25):125616.
[31] Zhang D, Liu R, Li Z. Irregular LIPSS produced on metals by single linearly polarized femtosecond laser. Int J Extrem Manuf 2022;4:015102 (11pp).
[32] Zhang DS, Sugioka K. Hierarchical microstructures with high spatial frequency laser induced periodic surface structures possessing different orientations created by femtosecond laser ablation of silicon in liquids. Opt Electron Adv 2019;2:190002.
[33] Sedao X, et al. Growth twinning and generation of high-frequency surface nanostructures in ultrafast laser-induced transient melting and resolidification. ACS Nano 2016;10:6995–7007.
[34] Rajendran R, Krishnadev ER, Anoop KK. Direct femtosecond laser processing for generating high spatial frequency LIPSS (HSFL) on borosilicate glasses with large-area coverage. Photonics 2023;10:793.
[35] Shi X, Xu X. Laser fluence dependence of ripple formation on fused silica by femtosecond laser irradiation. Appl Phys A 2019;125:256.
[36] Xu S-Z, Sun K, Yao C-Z, Liu H, Miao X-X, Jiang Y-L, Wang H-J, Jiang X-D, Yuan X-D, Zu X-T. Periodic surface structures on dielectrics upon femtosecond laser pulses irradiation. Opt Express 2019;27:8983.
[37] Rivera LP, Munoz-Martin D, Chávez-Chávez A, Morales M, Gómez-Rosas G, Molpeceres C. Subwavelength LIPSS formation on SS304 by picosecond laser irradiation under water confinement. Mater Sci Eng B 2021;273:115393.
[38] Lu M, Cheng K, Qin Z, Ju J, Liu J, Huo Y. Electromagnetic origin of femtosecond laser-induced periodic surface structures on GaP crystals. Opt Express 2022;30:10152.
[39] Gräf S, Kunz C, Engel S, Derrien TJY, Müller FA. Femtosecond laser-induced periodic surface structures on fused silica: the impact of the initial substrate temperature. Materials (Basel) 2018;11:5–7.
[40] Atwater HA, Polman A. Plasmonics for improved photovoltaic devices. Nat Mater 2010;9:205–13.
[41] Flemming RG, Murphy CJ, Abrams GA, Goodman SL, Nealey PF. Effects of synthetic micro- and nano-structured surfaces on cell behavior. Biomaterials 1999;20:573–88.
[42] Martinez-Calderon M, Manso-Silvan M, Rodriguez A, Gomez-Aranzadi M, Garcia-Ruiz JP, Olaizola SM, Martin-Palma RJ. Surface micro- and nano-texturing of stainless steel by femtosecond laser for the control of cell migration. Sci Rep 2016;6:36296.
[43] Stratakis E, Ranella A, Fotakis C. Biomimetic micro/nanostructured functional surfaces for microfluidic and tissue engineering applications. Biomicrofluidics 2011;5:013411.
[44] Yu E, Kim SC, Lee HJ, Oh KH, Moon MW. Extreme wettability of nanostructured glass fabricated by non-lithographic, anisotropic etching. Sci Rep 2015;5:9362.
[45] Skoulas E, Manousaki A, Fotakis C, Stratakis E. Biomimetic surface structuring using cylindrical vector femtosecond laser beams. Sci Rep 2017;7:45114.
[46] Bonse J, Rosenfeld A, Krüger J. On the role of surface plasmon polaritons in the formation of laser-induced periodic surface structures upon irradiation of silicon by femtosecond-laser pulses. J Appl Phys 2009;106:1–21.
[47] Martsinovskii GA, Shandybina GD, Smirnov DS, Zabotnov SV, Golovan LA, Yu-Timoshenko V, Kashkarov PK. Ultrashort excitations of surface polaritons and waveguide modes in semiconductors. Opt Spectrosc 2008;105:67–72.
[48] Florian C, Fuentes-Edfuf Y, Skoulas E, Stratakis E. Santiago Sanchez-Cortes 3, Javier Solis 1 and Jan Siegel, Influence of heat accumulation on morphology debris deposition and wetting of LIPSS on steel upon high repetition rate femtosecond pulses irradiation. Materials (Basel) 2022;15:7468.
[49] Yakovlev E, Shandybina G, Shamova A. Modelling of the heat accumulation process during short and ultrashort pulsed laser irradiation of bone tissue. Biomed Opt Express 2019;10:3030–40.
[50] Hammerschmidt U, Abid M. The thermal diffusivity of glass Sieves: II. Gas-saturated Frits. Int J Thermophys 2021;42:95.
[51] Shibata H, Suzuki A, Ohta H. Measurement of thermal transport properties for molten silicate glasses at high temperatures by means of a novel laser flash technique. Mater Trans 2005;46(8):1877. to 188.
[52] Eaton SM, Zhang H, Herman PR, Yoshino F, Shah L, Bovatsek J, Arai AY. Heat accumulation effects in femtosecond laserwritten waveguides with variable repetition rate. Opt Express 2005;13:4708.